

Supplement of

Inverse modelling of carbonyl sulfide: implementation, evaluation and implications for the global budget

Jin Ma et al.

Correspondence: Jin Ma (j.ma@uu.nl)

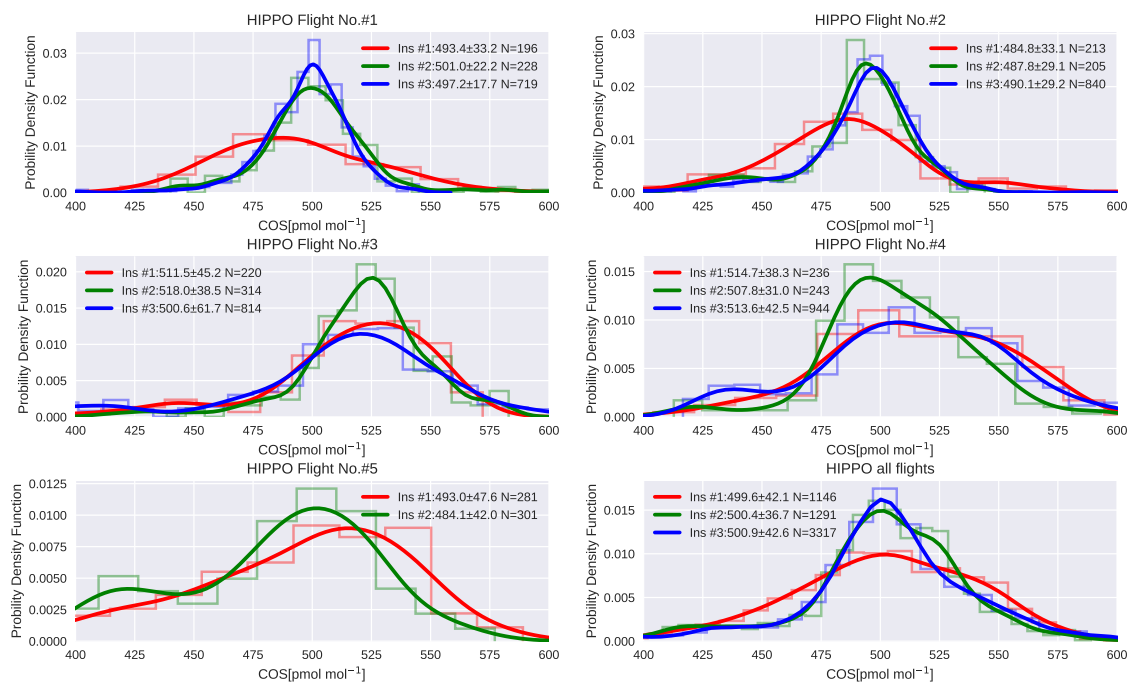


Figure S1. COS mole fraction distribution measured by HIPPO instruments 1–3. The measurements of COS were taken by 3 different instruments. The last panel represent the averages of all HIPPO flights. The mean and number of measurements of each flight are shown in legends.

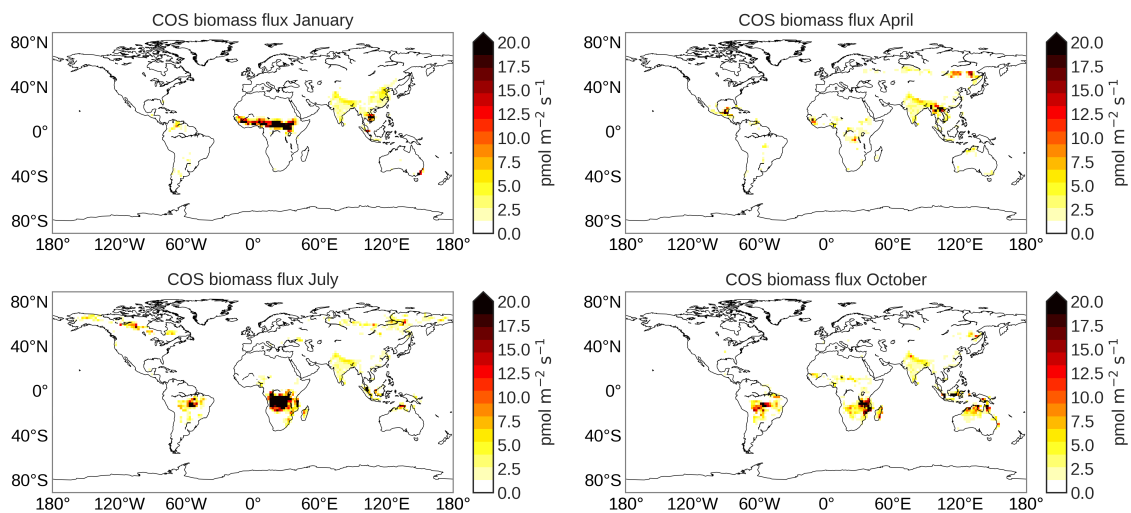


Figure S2. Spatial distribution of prior COS biomass burning fluxes for January, April, July, and October. Note that we use an extended colorbar due to hot spot emissions. The fluxes are averaged over the years 2000–2012.

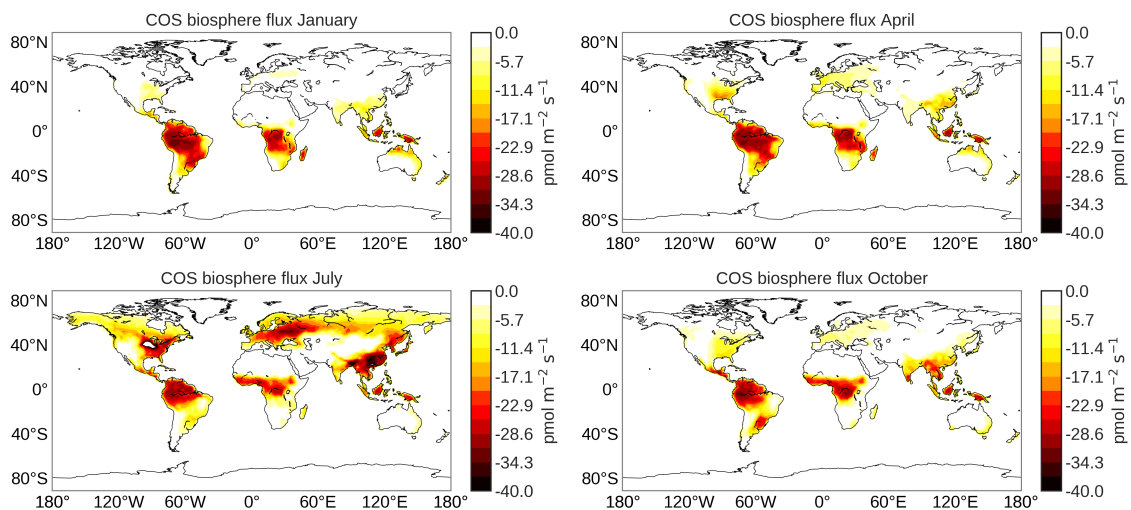


Figure S3. Spatial distribution of prior COS biosphere fluxes for January, April, July, and October. The fluxes are averaged over the years 2000–2012.

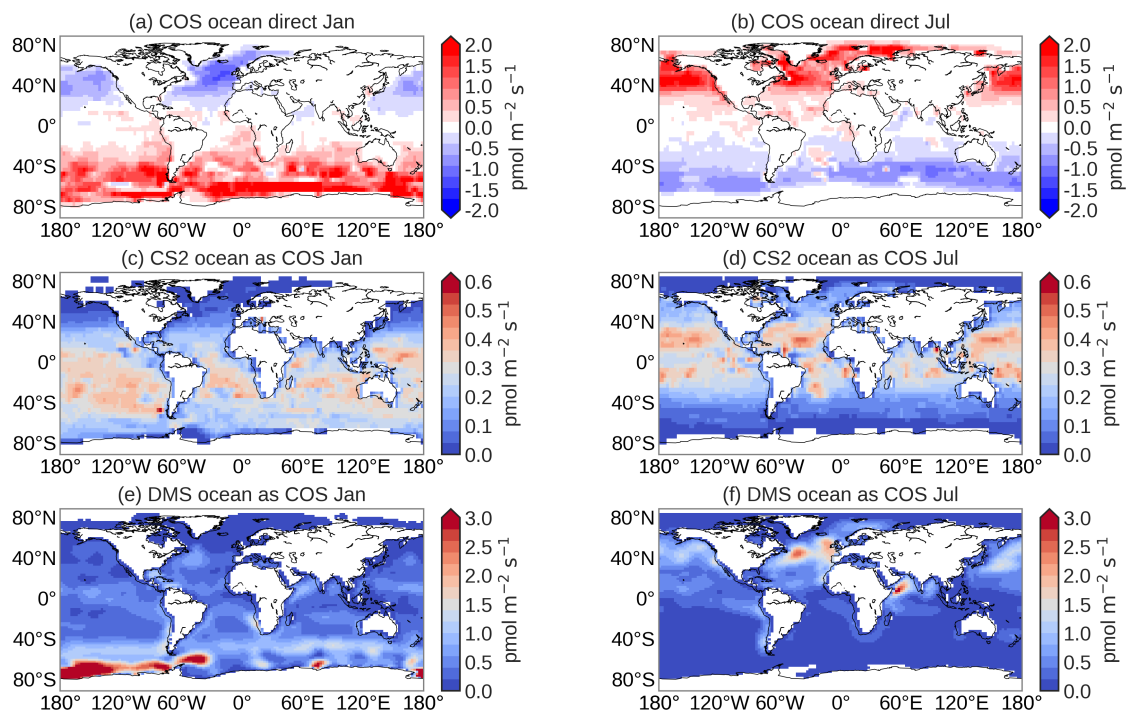


Figure S4. Spatial distribution of the climatological prior ocean fluxes of COS (upper), CS₂ (middle) and DMS (lower) for January (left) and July (right) based on Suntharalingam et al. (2008). Colorbars are extended with an arrow indicating that values may exceed the maximum or minimum value. Fluxes of CS₂ and DMS are converted to COS using yields of 83% and 0.7%, respectively.

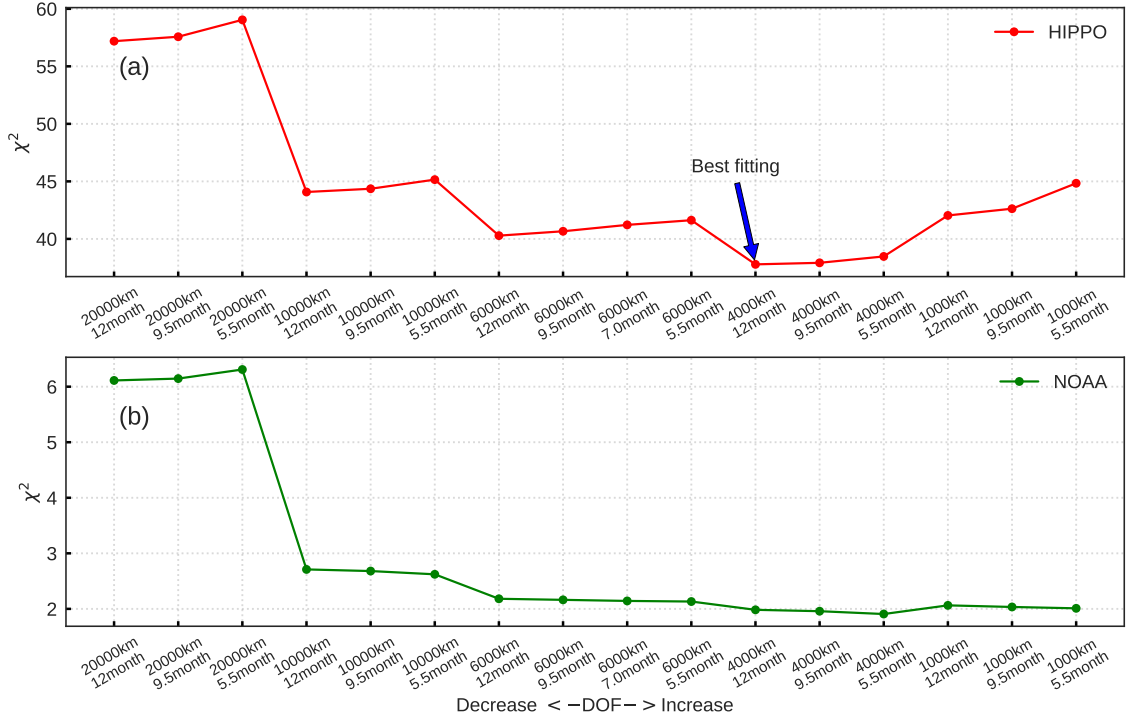


Figure S5. Spatial and temporal correlation settings in inversion S_u and the resulting χ^2 metric. (a) shows the comparison to HIPPO and (b) shows the χ^2 with respect to NOAA surface observations. The inversions were run for the years 2008–2011 and HIPPO campaigns 1-3 were sampled. The first and last 6 months of inversions were removed to calculate χ^2 . The arrow indicates the correlation setting selected for all further experiments.

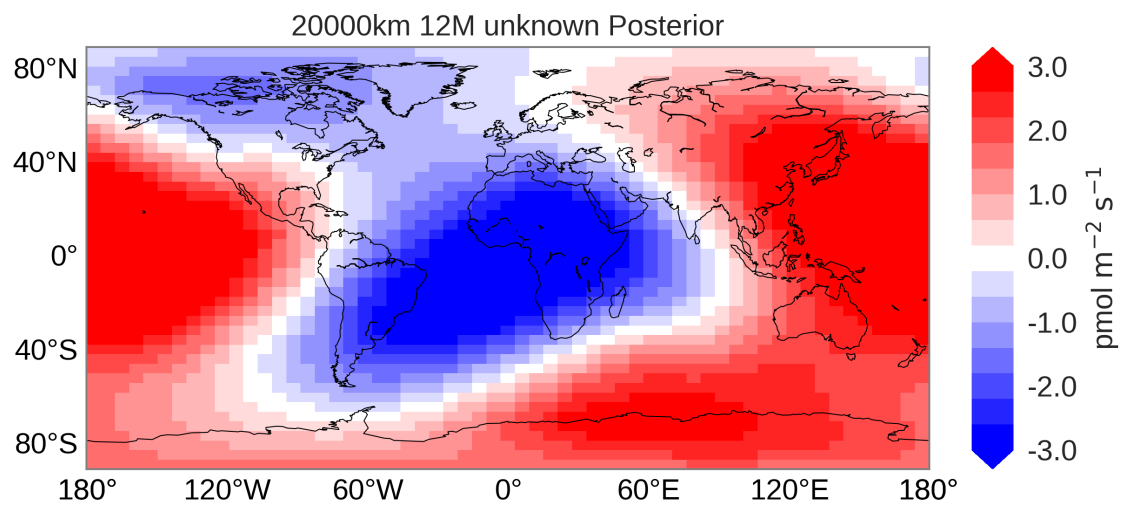


Figure S6. Optimized emission field of inversion S_u for a spatial correlation length of 20000 km and a temporal correlation length of 12 months. This field differs markedly from the optimized patterns presented in the main text.

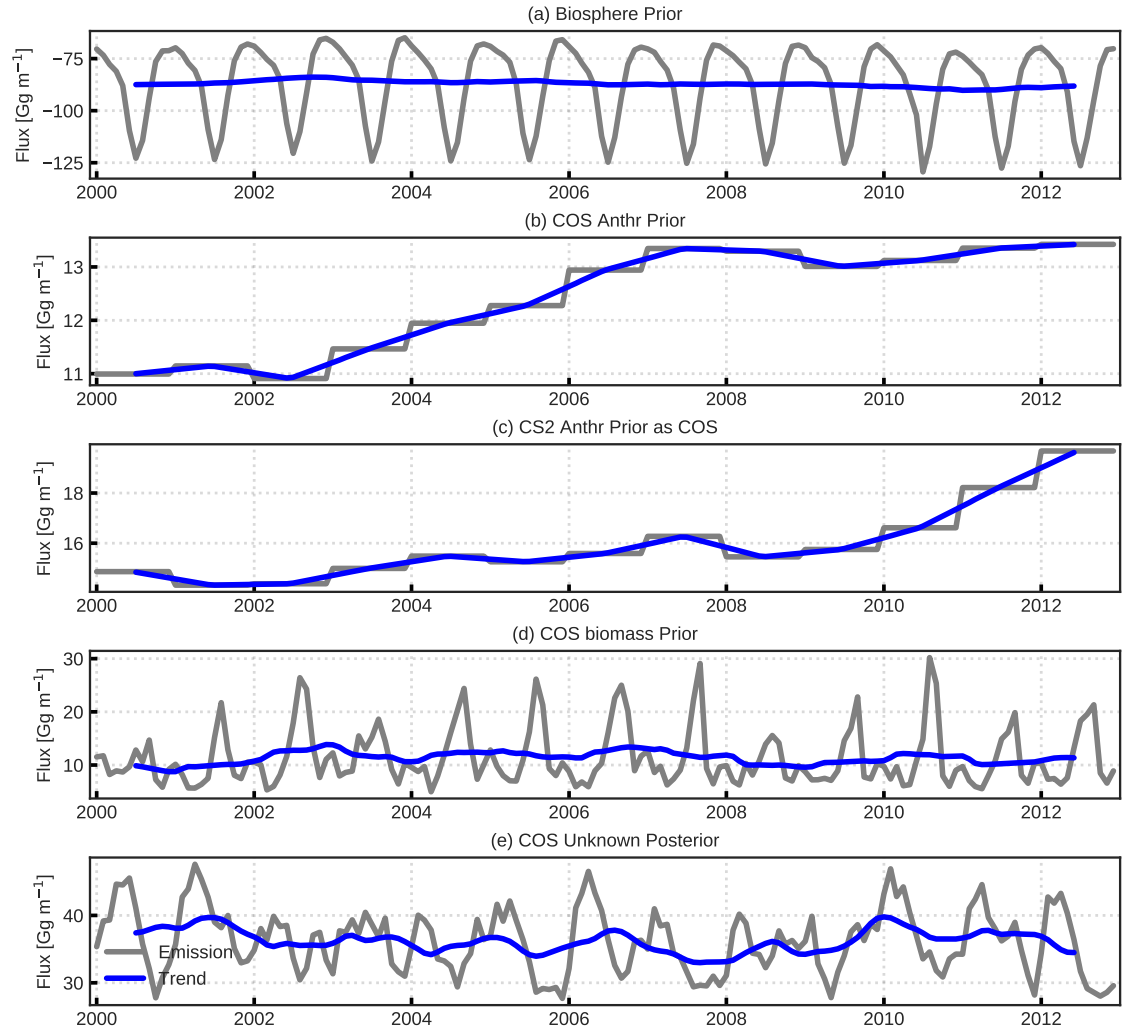


Figure S7. Monthly exchange fluxes related to inversion S_u : (a) prior biosphere (b) anthropogenic COS emissions (c) COS from anthropogenic CS_2 (d) biomass burning (e) optimized "unknown" emissions. Monthly global fluxes are shown in gray, and the trend is shown in blue.

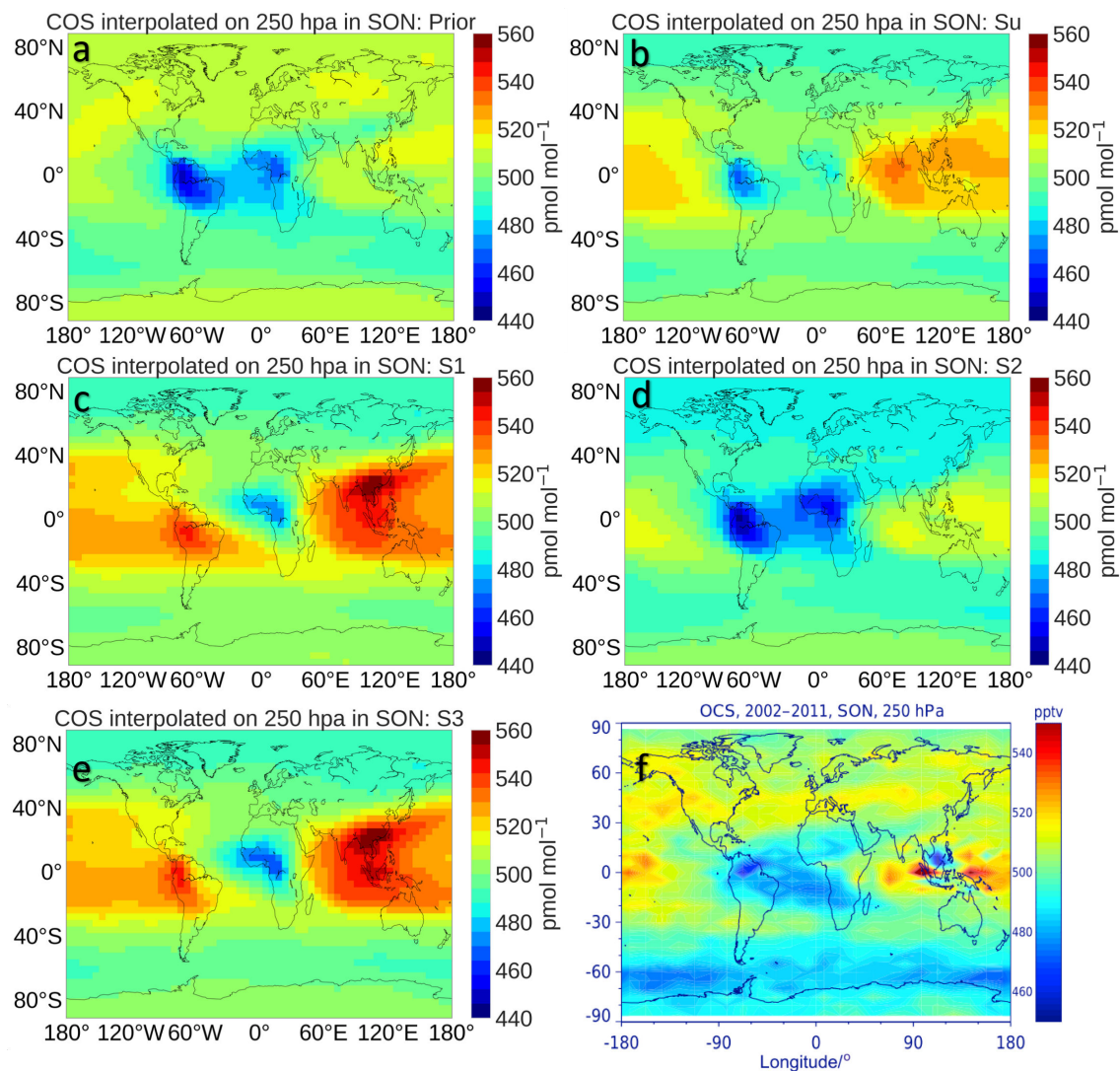


Figure S8. COS mole fraction comparison between MIPAS and TM5 on 250 hPa in September to November. (a–e) are TM5 prior, and inversions S_u , S_1 , S_2 , S_3 , respectively. (f) is captured from figure 11 in (Glatthor et al., 2017). TM5 results represent a 2008–2010 average, and MIPAS is averaged over 2002–2011. Because TM5 is systematically lower than MIPAS, 25 pmol mol^{-1} is added to the TM5 results for a better visual comparison.

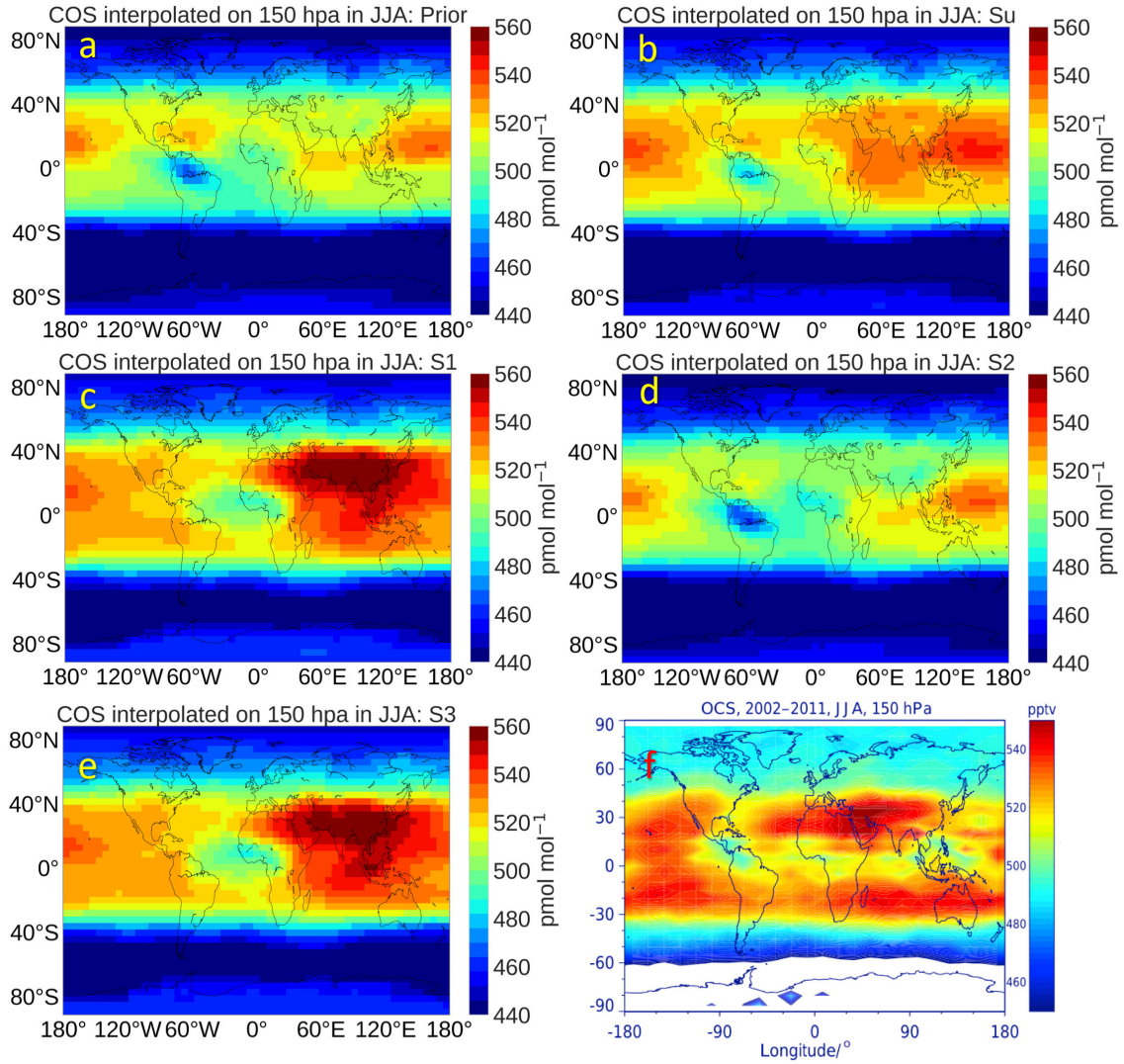


Figure S9. COS mole fraction comparison between MIPAS and TM5 on 150 hPa in June to August. (a–e) are TM5 prior, and inversions S_u , S_1 , S_2 , S_3 , respectively. (f) is captured from figure 12 in (Glatthor et al., 2017). TM5 results represent a 2008–2010 average, and MIPAS is averaged over 2002–2011. Because TM5 is systematically lower than MIPAS, 25 pmol mol⁻¹ is added to the TM5 results for a better visual comparison.

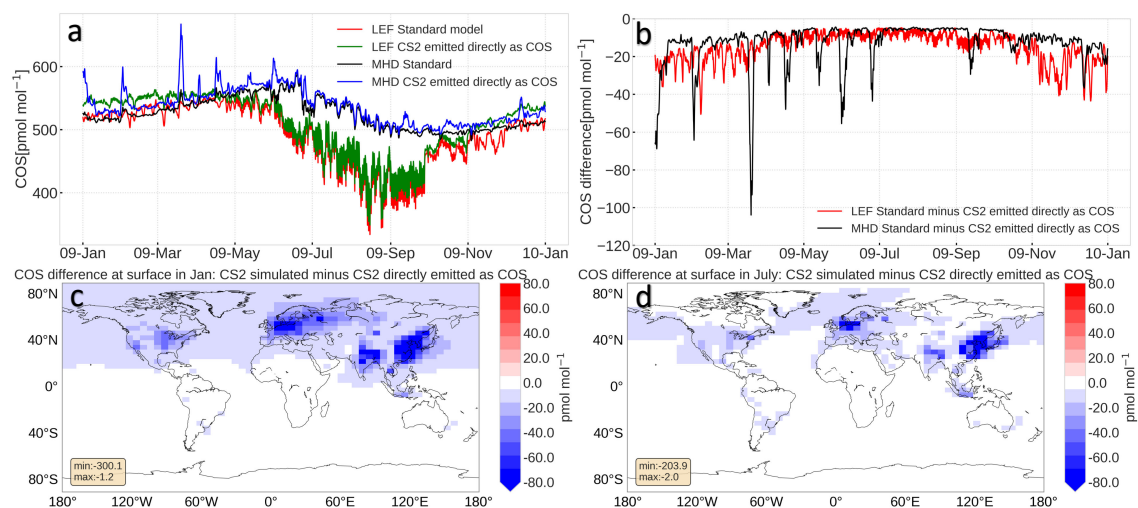


Figure S10. Sensitivity test in which CS₂ is emitted as COS compared to the standard model: (a) COS mole fractions sampled at two stations (LEF and MHD) (b) COS difference sampled at two stations (LEF and MHD) (c) COS spatial difference at the surface in January (d) COS spatial difference at the surface in July. Note that the results are from forward model simulations with prior fluxes in 2008–2010. For clarity, in panels a and b only results in 2009 are shown.

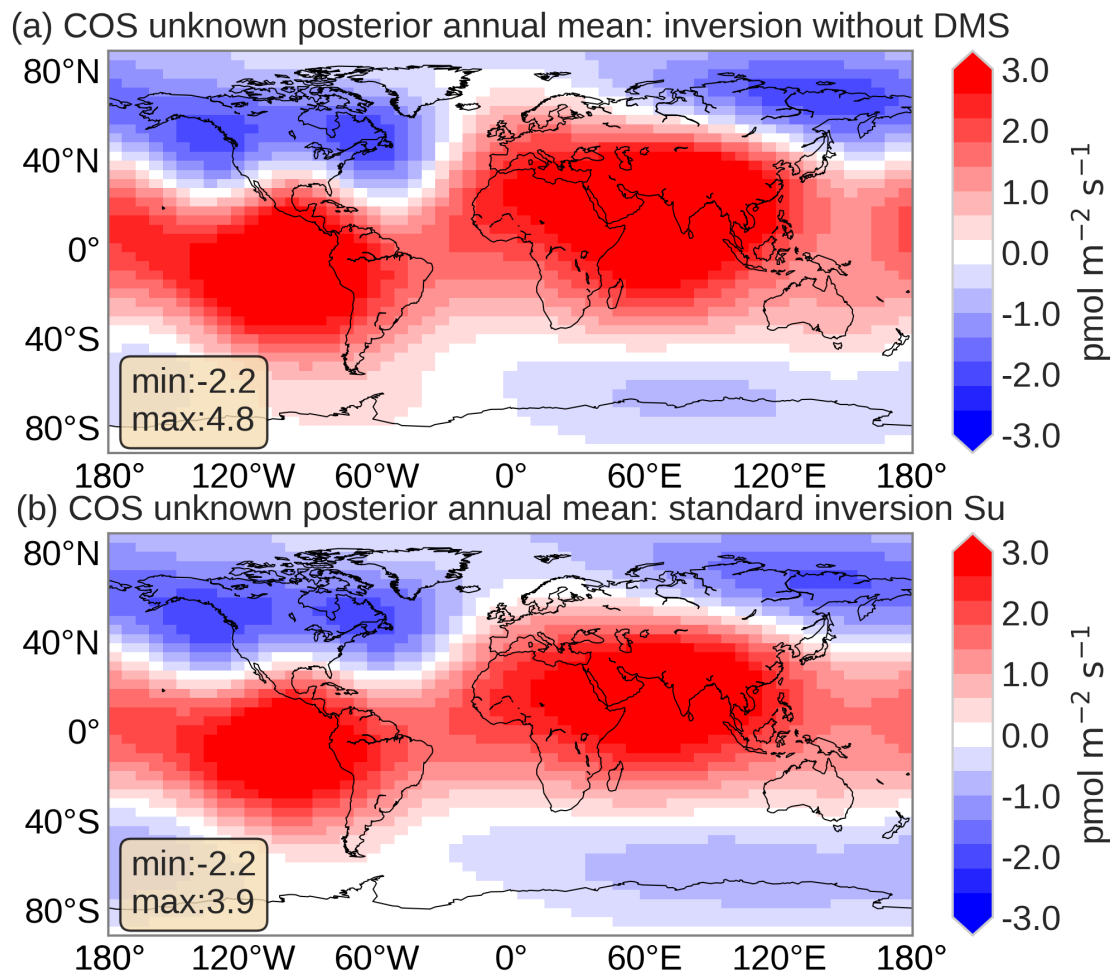


Figure S11. Posterior flux of the NO-DMS inversion and the standard inversion S_u : (a) posterior COS flux with DMS emissions added to the "unknown" flux (b) posterior COS flux from inversion S_u . The inversions have been performed for the year 2008-2010.

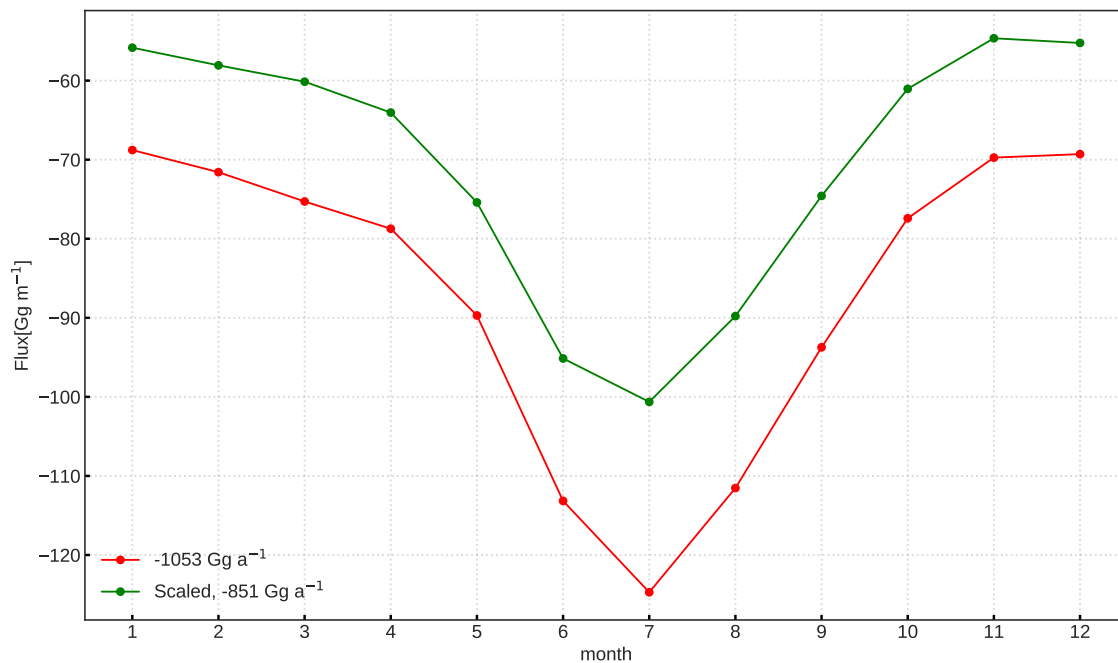


Figure S12. Monthly biosphere flux corrected by scaling with monthly-mean COS mole fractions (green) and the original biosphere flux calculated with a fixed mole fraction of $500 \text{ pmol mol}^{-1}$ used in the paper (red). The yearly-averaged corrected flux amounts to -851 Gg a^{-1} compared to -1053 Gg a^{-1} for the original flux.

Surface COS retrieved from inversion for months

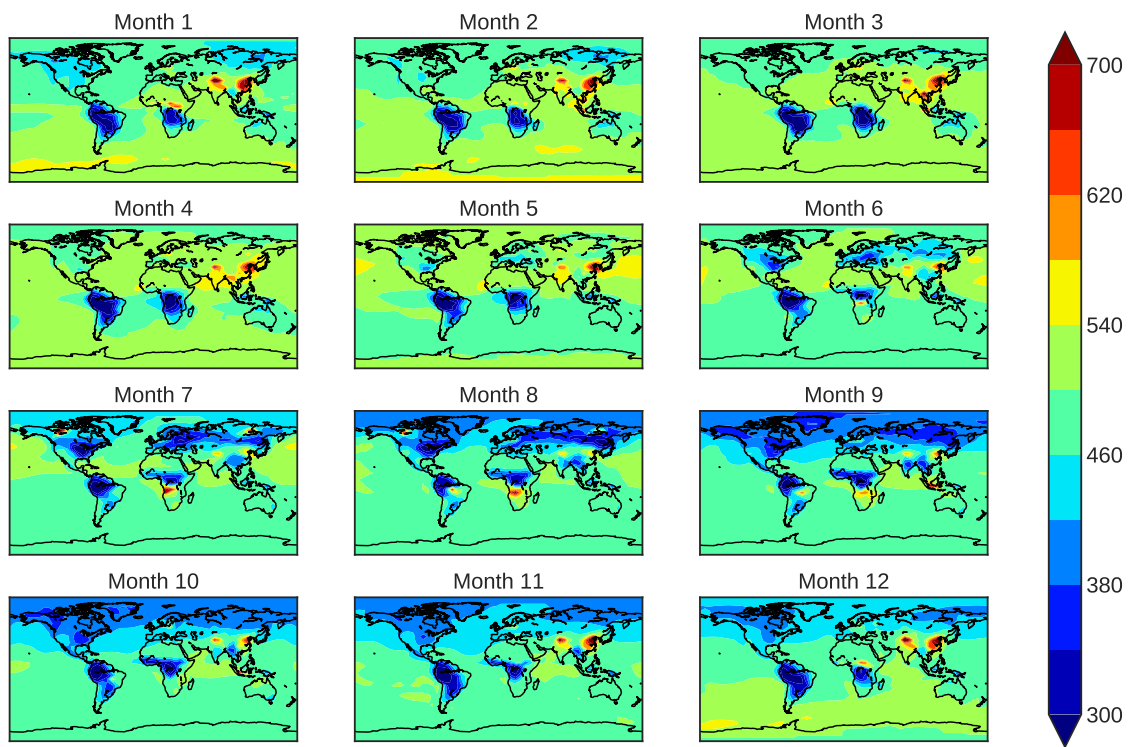


Figure S13. Monthly-mean surface COS mole fractions in pmol mol^{-1} from inversion S_u in the year 2018.

Scaling factor of biosp flux for months

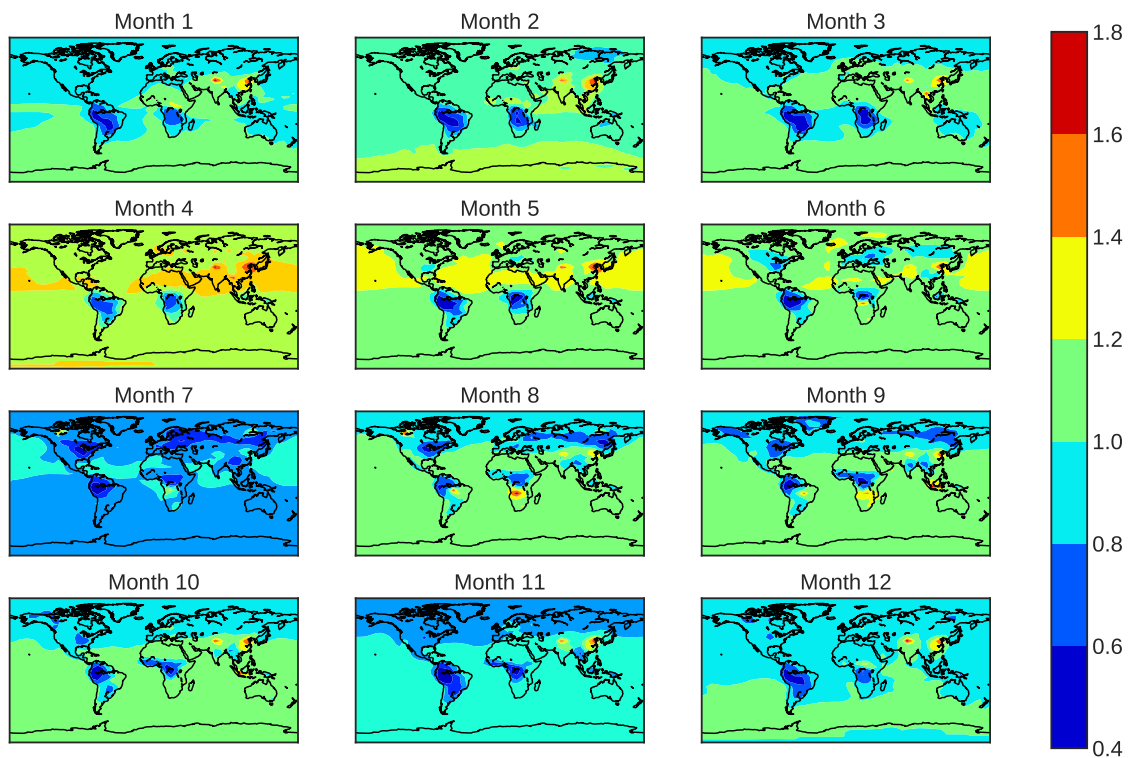


Figure S14. Monthly scaling factors for correcting the original SiB4 prior biosphere flux in the year 2018. The unit-less scaling is calculated as the monthly-mean surface COS mole fraction from Figure S13 divided by $500 \text{ pmol mol}^{-1}$.

Table S1. Prior and posterior fluxes, calculated errors, and error reduction of the different inversions for the 2008–2011 period, aggregated to global totals. Note that we removed the first and last 6 months from the inversions as spin-up and spin-down periods. CS₂ emissions are converted to COS indirect emissions using a conversion factor of 0.83. The correlation lengths for inversions S1–S3 are 4000 km and 12 months.

	Flux category	Grid-scale error	Prior (Gg a ⁻¹)	Posterior (Gg a ⁻¹)	Error Reduction
S _u	COS unknown ^a	100 %	432±20.2	436.7±3.8	81.4 %
	COS unknown ^b	100 %	432±25.5	436.7±3.5	86.3 %
	COS unknown ^c	100 %	432±99.0	443.1±7.3	92.6 %
	COS unknown ^d	100 %	432±284.6	423.2±5.2	98.2 %
S1	COS anthropogenic	10 %	157.3±6.9	154.7±6.7	2.4 %
	COS ocean	50 %	40.6±15.4	-15.7±11.8	23.4 %
	COS biosphere	50 %	-1053.1±165.3	-564.0±20.3	87.8 %
	COS biomass	10 %	122.5±4.6	118.7±4.6	0.2 %
	CS ₂ anthropogenic	10 %	190.7±8.1	189.7±8.0	2.1 %
	CS ₂ ocean	50 %	83.0±10.6	98.7±10.5	0.6 %
S2	COS ocean	50 %	40.6±15.4	24.9±6.3	59.0 %
	CS ₂ ocean	50 %	83.0±10.6	535.8±6.5	38.3 %
S3	COS biosphere	50 %	-1053.1±165.3	-613.2±7.1	95.7 %

^a Spatial and temporal correlation length: 1000 km and 5.5 months.

^b Spatial and temporal correlation length: 1000 km and 12 months.

^c Spatial and temporal correlation length: 4000 km and 12 months.

^d Spatial and temporal correlation length: 20000 km and 12 months.

Prior and posterior errors of exchange fluxes are aggregated to global totals and averaged in time by the TM5-4DVAR post-preprocessing (VPP) program, and the statistics are shown in Table S1. The method of error estimation was introduced by Meirink et al. (2008a, b). Because the inverse model system applied in this study is linear, the posterior errors can be estimated, as discussed in Meirink et al. (2008b). Error reduction (ER) is defined as:

$$ER = 1 - \frac{\sigma_{\text{post}}}{\sigma_{\text{prior}}}, \quad (\text{S1})$$

where σ_{post} denotes the posterior error, and σ_{prior} is the prior error. For inversion S_u, only the unknown source term is optimized with a prescribed grid-scale error of 100 %. With increasing spatial and temporal error correlations between the grid-scale prior fluxes, the global prior error increases. As a result, error reductions increase from 81 % (spatial correlation length 1000 km, temporal correlation lengths 5.5 month) to 98 % (20000 km and 12 months), because posterior errors on

10 the global budget closure are all in the range 3–8 %. The error reductions depend strongly on the magnitude of the flux and the error assigned to them. For instance, error reductions for the biosphere fluxes in inversions S1 and S3 are as high as 90 %, which is related to their large magnitude and the large prior error of 50 % assigned to the fluxes. Flux corrections and error reductions of the other S1 fluxes (anthropogenic, biomass burning) are small, indicating that insufficient observations are available to optimize these terms. In inversion S2, in which only oceanic sources were optimized, the error reductions are
15 smaller than for inversions S1 or S3, mostly because ocean fluxes are smaller in magnitude, and give less degrees of freedom to improve the match with observations, especially over land. Note further that some flux terms are optimized way outside the prior error range that was assigned to them. Generally, this indicates that structural model errors are present. In the case of COS, these structural errors are likely related to missing sources and sinks in the COS budget.

References

- 20 Glatthor, N., Höpfner, M., Leyser, A., Stiller, G. P., Von Clarmann, T., Grabowski, U., Kellmann, S., Linden, A., Sinnhuber, B. M., Krysztofiak, G., and Walker, K. A.: Global carbonyl sulfide (OCS) measured by MIPAS/Envisat during 2002-2012, *Atmospheric Chemistry and Physics*, 17, 2631–2652, <https://doi.org/10.5194/acp-17-2631-2017>, <https://hal-insu.archives-ouvertes.fr/insu-01557680/https://www.atmos-chem-phys.net/17/2631/2017/>, 2017.
- Meirink, J. F., Bergamaschi, P., Frankenberg, C., D’Amelio, M. T., Dlugokencky, E. J., Gatti, L. V., Houweling, S., Miller, J. B.,
25 Röckmann, T., Villani, M. G., and Krol, M. C.: Four-dimensional variational data assimilation for inverse modeling of atmospheric methane emissions: Analysis of SCIAMACHY observations, *Journal of Geophysical Research Atmospheres*, 113, D17 301, <https://doi.org/10.1029/2007JD009740>, <http://doi.wiley.com/10.1029/2007JD009740>, 2008a.
- Meirink, J. F., Bergamaschi, P., and Krol, M. C.: Four-dimensional variational data assimilation for inverse modelling of atmospheric methane emissions: Method and comparison with synthesis inversion, *Atmospheric Chemistry and Physics*, 8, 6341–6353,
30 <https://doi.org/10.5194/acp-8-6341-2008>, <https://www.atmos-chem-phys.net/8/6341/2008/>, 2008b.
- Suntharalingam, P., Kettle, A. J., Montzka, S. M., and Jacob, D. J.: Global 3-D model analysis of the seasonal cycle of atmospheric carbonyl sulfide: Implications for terrestrial vegetation uptake, *Geophysical Research Letters*, 35, L19 801, <https://doi.org/10.1029/2008GL034332>, <http://doi.wiley.com/10.1029/2008GL034332>, 2008.